Ocean Modelling
June 2023, Volume 183, Pages 102184 (14p.)
https://doi.org/10.1016/j.ocemod.2023.102184
https://archimer.ifremer.fr/doc/00823/93517/

A self-similar description of the wave fields generated by tropical cyclones

Yurovskaya Maria [1, 2, *], Kudryavtsev Vladimir [1, 2], Chapron Bertrand [3]

[1] Marine Hydrophysical Institute, Kapitanskaya st.,2, Sevastopol, 299038, Russia
[2] Russian State Hydrometeorological Institute, Malookhtinsky pr., 98, St. Petersburg, 195196, Russia
[3] Institut Francais de Recherche pour l'Exploitation de la Mer (IFREMER), 1625, route de Sainte-Anne, Plouzane, 29280, France

* Corresponding author : Maria Yurovskaya, email address : mvkosnik@gmail.com

Abstract :

Today, advanced operational wave models, e.g. WAM, SWAN or WAVEWATCH-III, provide very accurate solutions. Nevertheless, under extreme weather conditions, surface wave predictions can remain challenging. Indeed, for relatively small-scale tropical cyclones (TCs), rapidly evolving in time and space, and possibly not always well sampled with observing systems, extreme winds may not be properly described, and generated wave systems correctly predicted. In that context, Kudryavtsev et al. (2021b) recently proposed a simplified framework to rapidly assess evolving wave fields under typical TC conditions. Using self-similar functions, termed Tropical Cyclone-Wave Geophysical Model Function (TCW GMF), the proposed methodology and initial results demonstrate robustness and efficiency : 2D functions, assimilating a small number of parameters (maximum wind speed, cyclone radius and translation velocity), provide first-guess estimates of surface wave heights, wave lengths and directions within the intense TC core region. Following this strategy, an improved TCW GMF version is proposed to also cover the TC far zone, providing both wind wave information and outrunning swell conditions. This new version more particularly accounts for the wave field sensitivity to the shape of the wind profile. The procedure follows three main steps: (1) estimation of the characteristics of pure wind waves using self-similar matrices; (2) determination of the contour limiting the transition between wind waves to swell regime using empirically-derived universal functions; (3) derivation of analytical functions to describe the swell parameters using initial parameters estimated at this transition contour. Wind waves and swell systems are further superposed to describe the wave parameters for mixed-sea conditions. In this study, IBTrACS are used to initialize the TC's wind profiles, coordinates and translation velocities. The proposed methodology is then tested using a large altimeter database. More than 700 altimeter measurements crossing different TCs during 2020–2022 years are used, demonstrating overall convincing agreements between first-guess estimates and satellite data.

Graphical abstract

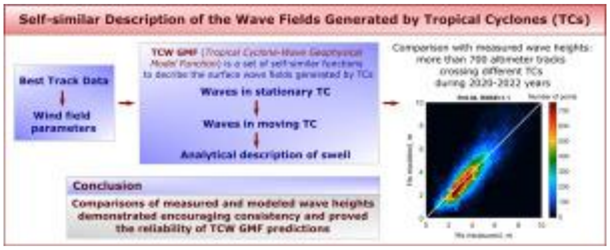

Highlights

► Self-similar functions to predict the wind waves within tropical cyclone core. ► Analytical expressions for swell outrunning a predicted self-similar contour. ► Best Track Data and multi-altimeter wave height observations to perform validation.

Keywords : tropical cyclones, self-similarity, wave height/wavelength field, swell, Best Track Data, altimeter constellation

1. Introduction

Annually, up to hundred tropical storms form. About half of them become strong hurricanes, with possible devastating impacts. Extreme wind events occupy an increasing place in the mass media, with direct social and economic implications (human loss, material destructions, etc.), also expected to become more destructive in the future as a consequence of global warming. Moreover, acknowledging their impacts on the coupled ocean-atmosphere system, marine-atmosphere extremes are key integral parts of the climate-change questions.

Tropical cyclone (TC) rapidly evolving characteristics are important, particularly, to reliably assess air-sea interaction processes. Numerical models still often fail to fully answer why different initial TC structures can result in different steady-state maximum intensities for what appear the same environmental conditions (Tao et al. (2020)). Coupled through the wave-dependent momentum flux, model analysis then often report significant impacts on the TC development and propagation track (Shimura et al. (2022)). Complex TC wave fields can indeed result in wave-induced stress misaligned with the surface winds, to affect the storm dynamics. From rapidly evolving wind speed and direction conditions, the presence of multiple, sometimes opposite, wave systems can indeed occur. Using improved wind inputs, advanced models, WAVEWATCH-III (Tolman (2009)), WAM (Hasselmann et al. (1988)), SWAN (Booij et al. (1999)) can now successfully forecast wave fields under extreme wind conditions (Kalourazi et al. (2021)). However, model resolutions may not always properly cope with small and rapidly evolving intense extreme events with localized large wind speed gradients. Consequently, swell waves radiating from intensive storms are reported to often be poorly predicted by forecast models, both in magnitude and arrival time (Babanin et al. (2019)).

For data-driven and/or ensemble methods for assimilation purposes, more simple and rapid solutions may then be considered to provide general surface wave characteristics, within the TC high intensity core, but also in far-field regions where swell systems originate and outrun. Given relatively simple and easy to parameterize forms of intense wind vortex, generally well-documented TC data from different weather services motivate to search for simple solutions for generated wave fields. Efforts already started from the middle of the last century (Bretschneider (1959); King and Shemdin (1987), see the review in Young (2017)). Today, combined with available satellite observations, parametric solutions seek to document the TC wind and wave conditions. Parametric solutions can then provide immediate first-guess estimates for the maximum wave height and wave length, and even 2D surface wave distributions.

These simplified methods essentially build on the extended fetch concept (Young (1988); Young and Vinoth (2013); Kudryavtsev et al. (2015)). Parametric solutions use self-similar expressions for wave height/length, similar to fetch laws for the case of wave development under uniform winds, originally suggested by Kitaigorodski (1962) and further specified in a number of experimental studies (see, e.g., Babanin and Soloviev (1998) and reviewed in Badulin et al. (2007); Zakharov et al. (2019)).

Presented by Kudryavtsev et al. (2021b) (hereinafter KYC21b), one of such solutions synthesizes results of wave simulations derived from a consistent 2D parametric wave-ray model Kudryavtsev et al. (2021a) (hereinafter KYC21a). Solutions, termed Tropical Cyclone-Wave Geophysical Model Function (TCW GMF), provide first-guess estimated fields of wave height, wave length and wave direction inside a given TC, prescribed by its maximum wind speed u_m, radius R_m and translation velocity V. The 2D parametric model and self-similar solutions were tested using multi-mission satellite observations for the hurricane Goni (2020) (Yurovskaya et al. (2022)). Results demonstrate very encouraging comparisons with measurements, including wave directional properties derived from CFOSAT SWIM instrument (Hauser et al. (2021); Aouf et al. (2021)).

Originally designed to describe the primary wave system (the longest wave) parameters in the TC inner core area, this TCW GMF is limited to radii less than 2-3 R_m. In this paper, the main objective is to propose a new version to extend these 2D self-similar solutions, not solely constrained to the TC core area, but valid at larger distances from the TC eye. The proposed self-similar solutions are further complemented by analytical solutions for swell systems, outrunning the inner area and propagating in different directions away from the moving TC. Combined, self-similar and analytical solutions then provide a simple, rapid, and self-consistent description of mixed seas in a TC region.

The arrangement of the paper is as follows: self-similar solutions for wind waves generated by a stationary TC and their transformation into swell systems escaping the inner storm area, are presented in Section 2, extension of these self-similar solutions for a moving TC is given in Section 3. Section 4 summarizes the model, and its input and output parameters. Comparisons between the model predictions and multi-satellite altimeter significant wave height (Hs) measurements are given in Section 5. Section 6 summarizes results of the paper.

2. Wave Self-similarities for Stationary TCs

Throughout this study, a TC wind field is prescribed in the axi-symmetric form suggested by Holland (1980):

$$u(r) = \sqrt{(u_m^2 + u_m R_m f)\left(\frac{R_m}{r}\right)^B \exp\left(-\left(\frac{R_m}{r}\right)^B + 1\right) + \left(\frac{rf}{2}\right)^2} - \frac{rf}{2}, \quad (1)$$

where f is the Coriolis parameter; r is distance from the TC center; u_m is maximum wind speed, R_m is the radius of maximum winds; B is the wind profile shape parameter varying (in the present study) within the range 0.5-2.5. A constant surface wind inflow angle is assigned. The wind vector is thus everywhere directed 20^o (inflow angle towards the TC eye) from the tangent axi-symmetric flow (e.g., Zhang and Uhlhorn (2012)). Though inflow angle variations can affect the resulting wave fields, we do not account them in this study, only considering the most typical case.

For a prescribed wind field, stationary in this Section, or moving with a translation velocity V, Section 3, numerical calculations of the wave field parameters (energy, wavelength and wave direction) are performed using the 2D parametric wave-ray model proposed in KYC21a. In total, more than 400 runs were performed for different combinations of wind field parameters, i.e. u_m ranging form 30 to 70 m/s, R_m from 10 to 100 km, V from 0 to 12 m/s and B from 0.5 to 2.5. Resulting wave-ray distributions were interpolated on a uniform grid, taking the parameters of the wave-train with maximum wavelength inside each grid cell. This is done for both wind waves and swell systems. Pure wind waves are further analysed to determine self-similar relations for 2D TC cases, using self-similar scaling arguments suggested by Kitaigorodski (1962) for a stationary TC, and those by Kudryavtsev et al. (2015) for a moving TC.

2.1. Wind Waves Development

2.1.1. Significant Wave Height and Wavelength

Demonstrated in KYC21b, their Fig.6, space-time evolution of wave parameters in a TC occurs from the vicinity of maximum winds towards the periphery. It is thus natural to relate the wave fetch with the TC radius. Considering a stationary TC case, it is tempting to check whether the classical scaling arguments suggested by Kitaigorodski (1962), solely based on local wind velocity u, distance from TC eye r and gravity acceleration g, are capable to reproduce 2D numerical simulations. More specifically, can these solutions apply for a wide range of TC radii, wind speed velocities, and diverse wind profile parameter B?

As first guess estimates, the peak wave height H and wavelength λ, scaled by the local wind speed and gravity, u^2/g, can be suggested to follow the fetch laws, similar to those under uniform wind conditions (Kitaigorodski (1962)):

$$\begin{aligned} Hg/u^2 &= 4c_e^{1/2} {r_d}^{p/2}, \\ \lambda g/u^2 &= 2\pi c_a^{-2} {r_d}^{-2q}, \end{aligned} \qquad (2)$$

where the dimensionless distance from the TC center $r_d = rg/u^2$ formally plays the role of fetch, despite the fact that the wind is not constant and not always aligned with the waves; c_e, c_a, p and q are empirical constants. These relationships should be valid for developing waves, i.e. while their inverse wave age $a = u_{||}/c_p$ is $a > a_0 = 0.85$, with c_p the phase velocity of the spectral peak, and $u_{||} = u\cos(\varphi_w - \varphi)$ the wind vector projection to the peak wave propagation direction.

At $u_{||}/c_p = a_0$, wind waves become fully developed and their wave height and wavelength saturate to H_{fd} and λ_{fd}, respectively:

$$\begin{aligned} H_{fd} g/u^2 &= 4c_e^{1/2} c_a^{-p/2q} a_0^{p/2q}, \\ \lambda_{fd} g/u^2 &= 2\pi/a_0, \end{aligned} \qquad (3)$$

solely dependent on local wind speed. Accordingly, at the TC periphery, wind waves are aligned with the wind and their heights and wavelengths proportional to u^2.

Fig. 1a,b show results of the 2D parametric model simulations with more than 50 combinations of R_m, u_m and B. Model simulations of significant wave height, Hs, and wavelength, scaled by g/u^2, are found to be well described with universal functions of the dimensionless distance from TC eye, rg/u^2, close to (2)-(3). Though these self-similar fetch laws (2)-(3) were originally derived for uniform wind conditions, they are surprisingly valid for spatially non-uniform TC wind field, Fig. 1a,b.

Fits of simulated data using (2)-(3) allow to specify the constants c_e, c_a, p and q for different TC conditions: $c_e = 0.65 \cdot 10^{-6}$, $c_a = 11.5$, $p = 0.87$, $q = -0.27$. These values are not very different from original ones used to implement the 2D parametric model ($c_e = 1.4 \cdot 10^{-6}$, $c_a = 11.8$, $p = 0.75$, $q = -0.25$). To describe a smooth transition to saturation, corresponding to a fully developed state, expressions (2) and (3) are combined to

$$H_0 = H_{fd} \tanh(H/H_{fd}) \tag{4}$$
$$\lambda_0 = \lambda_{fd} \tanh(\lambda/\lambda_{fd}),$$

where H_0 and λ_0 are the estimates of peak wave height and wavelength of wind waves, either fully developed or not. Fits, corresponding to (4), are shown with black solid lines on Fig. 1a,b.

Note, the suggested parameterizations for the wind wave Hs and wavelength for a stationary TC differ from those proposed in KYC21b for the longer waves. Unlike KYC21b, parameterizations (2)-(3) are now valid for wind waves, either located in near and far zones of a TC. Moreover, these parameterizations apply for arbitrary wind profile shape parameters B.

2.1.2. Wind Wave Directions

Based on the same simulations, the distribution of the wave to wind direction, obtained for pure wind waves, is shown on Fig. 1c versus the dimensionless radius $r_d = rg/u^2$. In contrast to wavelength and wave height parameters, the wave direction cannot be universally described for different combinations of R_m, u_m at $r_d \lesssim 1e4$ (see the color indicating $\tilde{R}_m = R_m g/u_m^2$). Furthermore, two regimes are clearly distinguished in Fig. 1c. A first regime takes place at $r_d < (1-5) \cdot 10^3$ where wind waves develop outward from the TC eye until they turn into swell. In this case, wind wave direction gradually deviates from the wind one. The second regime takes place at $r_d > (1-5) \cdot 10^3$ where the wind wave direction gradually tends (towards TC periphery) to be aligned with the wind. These waves represent systems of almost developed wind waves that travel along the wind direction in the far zone of the

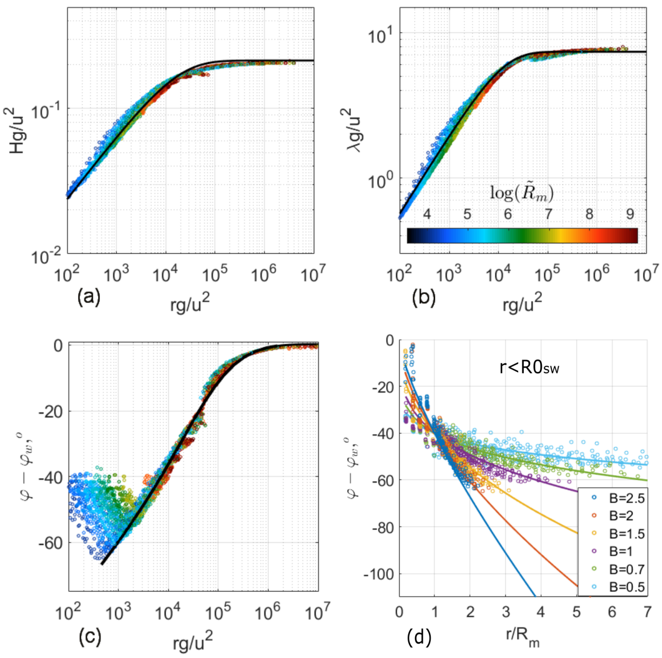

Figure 1: Distributions of scaled wave height (a), wavelength (b), and wind direction (c), versus distance from TC center scaled by local wind speed and gravity. Dots are results of numerical simulations, black solid lines are fits (4) for wave height and wavelength and (5) for wind to wave direction at $r > R0_{sw}$. (d) Wave to wind direction at $r < R0_{sw}$ scaled by radius of maximum winds for different wind shape parameter B, and respective fits (5).

cyclone. These systems are superimposed to longer swell ones arising from wind waves developing within the TC inner region, and propagating to the far zone. It leads to mixed sea conditions. The transition between these two regimes is quite smooth in terms of the dimensionless wave length and height parameters (Fig. 1a,b), but sharp in terms of the wave directions (Fig. 1c).

The fit of 2D parametric model, simulations of wind waves direction φ relative to the local wind direction, φ_w is then suggested to be expressed as:

$$\varphi - \varphi_w = a(r/R_m)^n, \;\; r < R0_{sw} \qquad (5)$$
$$\varphi - \varphi_w = (\varphi_0 + b \log \frac{r_d}{\tilde{r}_0}) \cdot Hev, \;\; r > R0_{sw}$$

with

$$a = -40^o, \; n = 0.3B, \; \varphi_0 = -80^o, \; \tilde{r}_0 = 100, \; b = 8,$$
$$Hev = 0.5 \cdot (1 - \tanh[0.4 \log \frac{r_d}{8 \times 10^4}]).$$

According to (5), a transition between regimes of wind waves, growing/decaying with distance from the TC center, occurs at radius $R0_{sw}$. It also corresponds to the transition of wind waves to swell. A parameterization of $R0_{sw}$ will be given below, in Section 2.2.2.

At $r < R0_{sw}$, the direction of developing wind waves is universally described in terms of r/R_m, with a power exponent n depending on the wind shape parameter B, Fig. 1d. At larger radii, $\varphi - \varphi_w$ are scattered if plotted versus r/R_m for different TC parameters (not shown), but converge in terms of r_d, Fig. 1c, solely depending on the local wind speed and distance from the TC center.

Eqs. (4) and (5) provide wind wave characteristics at any distance from a TC center and considered wind profiles. Note, the wind shape parameter B is not needed to describe wave height and wavelength, i.e. the local relations Eqs. (2)-(3) work for a variety of B. Hence, these relations can be extended to an arbitrary Holland-like wind profile without the need of an exact fit (1). However, for the wave direction, R_m, u_m and B must be specified and are required to determine $R0_{sw}$ and to use Eq. (5) at $r < R0_{sw}$. Fixing the wind shape parameter at $B = 1.5$ leads to an error in the wave direction less than 20^o (if $R0_{sw}$ is determined correctly), Fig. 1d, which can still be tolerated if exact information about B is missing.

2.2. Swell systems

Trajectories of wind wave trains developing within the TC inner region display unwinding spirals towards the outer region. At some distance $R0_{sw}$ from the TC eye, the local inverse wave age, $\alpha_{||}$, reaches a critical value (about 0.85), and the wave train start to travel like a swell system.

2.2.1. Swell Wavelength, Energy and Direction

Swell wave energy and wavelength along a swell-ray trajectory can be derived, within the KYC21a model framework, with the wind energy input switched off. Analytical solutions are given in Yurovskaya et al. (2022), Appendix A.3. Below, these final relations are repeated to be readily used to describe evolution of wave height H_{sw}, wavelength λ_{sw} and direction φ_{sw} along the swell-ray trajectory:

$$\begin{aligned}(H_i/H_{sw})^4 &= (\chi^2+\delta^2)\Big[\frac{1}{1+\delta^2}+\frac{A}{\delta}\Big(\arctan\frac{\chi}{\delta}-\arctan\frac{1}{\delta}\Big)\Big],\\ (\lambda_{sw}/\lambda_i)^5-1 &= \frac{b}{4}\ln\Big[1+A\frac{1+\delta^2}{\delta}\Big(\arctan\frac{\chi}{\delta}-\arctan\frac{1}{\delta}\Big)\Big],\\ \varphi_{sw}-\varphi_i &= 0\end{aligned}\qquad(6)$$

where indices "i" indicate initial wave parameters; l is the along-trajectory distance from initial point, $\chi = 1 + G_{ni}l$, $G_{ni} = (d\varphi/dn)_i$ the cross-ray gradient of wave rays directions; $\delta = 0.5\Delta c_g/\bar{c}_g = 0.1$, standard deviation of group velocity scaled by its mean value weighted over a JONSWAP-like spectrum; $A = 4(k_i/G_{ni})(k_ie_i/\varepsilon_T^2)^2$, $k_i = 2\pi/\lambda_i$, $e_i = H_i^2/16$, $\varepsilon_T^2 = 0.155$; $b = 0.59$.

For an axi-symmetric wind field with inflow angle φ_{inflow} (20^o in this study), swell direction, $\varphi_{sw} = \varphi_i$, relative to the wind one, φ_w, depends on distance from a TC eye, r, as

$$\varphi_{sw}-\varphi_w = -\arccos\left[\frac{R0_{sw}}{r}\cos(\varphi_i-\varphi_{inflow})\right]-\varphi_{inflow}. \qquad (7)$$

Note, omitting the effect of wave rays focusing/defocusing, $G_{ni}\to 0$, and expanding $\arctan(\chi/\delta)$ in the Taylor series, $\arctan(\chi/\delta) = \arctan(1/\delta) + \delta(\chi-1)/(1+\delta^2)$, the two first relations of Eqs. (6) can be simplified to:

$$\begin{aligned}(H_i/H_{sw})^4 &= 1+A(\chi-1) = 1+\pi^5/2\epsilon_T^4\cdot H_i^4\lambda_i^{-5}l \qquad (8)\\ (\lambda_{sw}/\lambda_i)^5 &= 1+\frac{b}{4}\ln[1+A(\chi-1)] = 1+\frac{b}{4}\ln[1+\pi^5/2\epsilon_T^4\cdot H_i^4\lambda_i^{-5}l],\end{aligned}$$

which are equivalent to Eqs. (12) of KYC21b with slightly different empirically derived constants. Yet, we emphasize that taking into account the cross-ray gradient of the wave train directions is of decisive importance. Indeed, this term ensures the attenuation of the energy $\propto l^{-1}$ with distance.

Relations (6)-(8) give Hs parameters to asymptotically decay more rapidly than weak-turbulent solutions Zaslavskii (2000); Badulin and Zakharov (2017). These authors considered Hasselmann (1962) kinetic equation for weakly nonlinear deep water waves in the absence of dissipation and external forcing, leading to a swell decay with fetch x, $H \sim x^{-1/6}$, $\lambda \sim x^{1/6}$, respectively. Our model predicts stronger energy attenuation due to wave dissipation and ray defocusing effects. Yet, weak-turbulent solutions can be recovered in KYC21a model framework. Indeed, while nonlinear interactions vanish after integration the energy balance equation over all wavenumbers, they are essential to govern the spectral peak frequency downshift. The stationary form of Eq. (48) of KYC21a for group velocity c_g,

$$c_g dc_g/dx \sim g(k^2 e)^2,$$

together with the stationary solution of their Eq. (47) for energy e in absence of forcing/dissipation and angular divergence term,

$$e = e_0 c_{g0}/c_g,$$

gives

$$c_g dc_g/dx \sim (e_0 c_{g0})^2 g^5 c_g^{-10}$$

(k is peak wavenumber, g - gravity, e_0, c_{g0} - undefined constants).

Solution of these equations is straightforward and reads

$$c_g \sim x^{1/12}, \lambda \sim x^{1/6}$$
$$H \sim \sqrt{e} \sim x^{-1/6}.$$

It corresponds to an energy flux conservation, $c_g e = \text{const}$, and coincides with Badulin and Zakharov (2017) solutions. Yet, these asymptotic estimates predict very weak decay, and are "absorbed" in (6)-(8) by stronger attenuation mechanisms included in the present model.

Already discussed, e.g., in Young (2006, 2017), non-linear wave-wave interactions can influence the wave directional spectrum formation in presence of swell, stabilizing the spectral shape to make it similar to fetch-limited cases. Young (2006) revealed that swell overlapping the local wind-sea in hurricanes often results in a directionally skewed spectrum, providing smooth transition between the dominant low-frequency swell and the high-frequency wind-sea components. Omnidirectional spectrum exhibits the features inherent to uni-directional wind case. Based on these observations, it was suggested, that the balance between the wind forcing, the nonlinear wave interactions and dissipation is not necessary to maintain such spectral shape. The action of nonlinear interactions is itself capable of bringing a complex mixture of locally generated wind waves and remotely generated swells to a spectrum that has a shape typical for uni-directional wind seas.

In our approach, swell (6) is considered separately from the underlying wind waves, and thus we do not account for the effects of their interactions. On the other hand, a smooth transition in spectral directional spreading functions from swell to wind seas was also found in (KYC21b, see their Fig.13), where the spectral shape was formed through superposition of parameters of "independent" wave trains crossing a given area.

2.2.2. Wind Waves-to-Swell Transition Point

The swell initial parameters in Eqs. (6)-(7), wave height H_i, length λ_i and direction φ_i, should match the corresponding parameters of wind waves, (4)-(5), at radial distance $R0_{sw}$, where the inverse wave age of wind waves reaches the threshold value $u_{||}/c_p = 0.85$.

From simulations, $R0_{sw}/R_m$, obtained for different TC parameters, is plotted versus dimensionless TC radius $\tilde{R}_m = R_m g/u_m^2$, Fig. 2a,b,c, for three values of the shape parameter B. The distributions accurately follow the power law:

$$R0_{sw}/R_m = r_a(\tilde{R}'_m/\tilde{R}_m)^b, \tag{9}$$

with $\tilde{R}'_m = 10^4$, $r_a = 1.2$ and b depending on wind shape parameter.

Approximated using simulations with 6 different values of B, Fig. 2d, the power b in (9) depends on B as

$$b = 0.27B^{-0.85}. \tag{10}$$

For $B = 1.5$, Eq. (9) with Eq. (10) reads: $R0_{sw}/R_m \approx 7\tilde{R_m}^{-0.2}$. It is the same power law, but with coefficient 15% larger, than the relation suggested by KYC21b (their Eq. (10): $r/R_m = 5\tilde{R_m}^{-0.2}$), where only TC cases with $B = 1.5$ were considered.

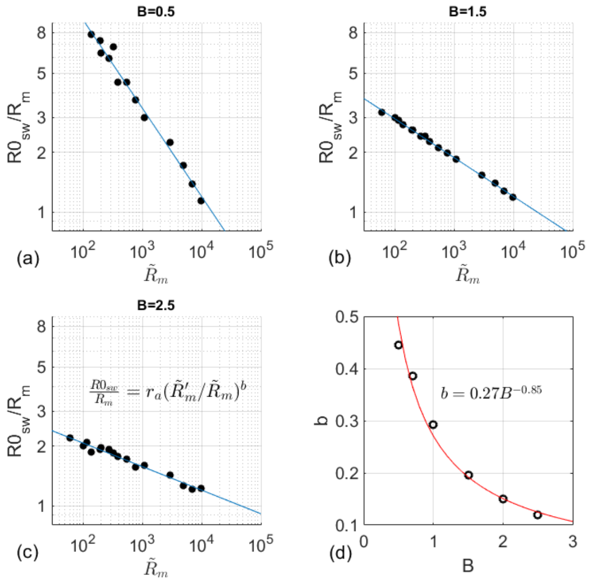

Figure 2: (a)-(c) Normalized distance from the center of a stationary cyclone to the point where $u\cos(\varphi - \varphi_w)/c_p = 0.85$ versus $\tilde{R_m} = R_m g/u_m^2$ in simulations with different values of Holland parameter B. (c) Power b in approximation (9) versus B

The threshold $u_{||}/c_p = 0.85$ to define $R0_{sw}$ is quite arbitrary. A more realistic transition between wind waves and swell using 2D parametric model simulations is not sharp. It is due to the smooth attenuation of wind energy input close to regions where $u_{||}/c_p = 0.85$, around which (before and after), wind waves still gain some wind energy. Accurate determination of $R0_{sw}$ may impact the swell parameters, Eqs. (6), which are ultimately linked to wind waves parameters H_i and λ_i, defined through Egs. (4) at radius $R0_{sw}$. Comparisons between analytical approximations with direct numerical calculations then reveal that the factor 0.85 to define $R0_{sw}$ (Eq. (9)) may be sufficient to bring analytical solutions in line with full model simulations for wave development under stationary TC conditions.

2.3. TCW GMF Performance for Stationary TCs

Following the suggested approximations, resulting wave characteristics for stationary TC conditions are shown Fig. 3, for wind profiles with different values of R_m and u_m and $B = 1.5$. Following KYC21b (their Fig. 15), wavelength and wave height estimates are scaled using R_m, u_m, g and fetch laws exponents p, q, and displayed versus normalized local radius r/R_m. Stars and triangles indicate simulated wind and swell waves, respectively; solid lines are obtained using self-similar expressions (4)-(5) for wind waves and analytical solutions for swell, generated at radius $0.85R0_{sw}$, $R0_{sw}$ obtained from Eq. (9). Suggested fits accurately predict the wave parameters distributions. Note, while derived for $r > R_m$, relations (4)-(5) also apply for smaller radii, Fig. 3. Fitted and numerically simulated wave characteristics are also found in consistent agreement for other values of B.

3. Wave Self-Similarities for Moving TC

TC motions may strongly influence the wave developments in different sectors relative to the TC heading. TC motions lead to asymmetrical wave fields, even for a perfectly axi-symmetric wind field. In the right sector (left in Southern hemisphere), wind direction and developing waves almost align with TC heading. Waves can longer be exposed to strong winds - this is a so called wave trapping phenomenon (Dysthe and Harbitz (1987); Young (1988); Bowyer and MacAfee (2005)), causing strong wave intensification in the right-front sector compared to a stationary TC condition. In the left sector, wind direction and developing waves are opposite to TC heading. The residence time of waves in the storm area is reduced, i.e. waves are

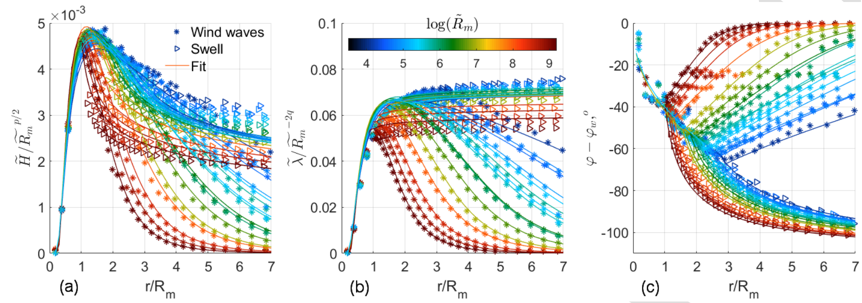

Figure 3: Radial profiles of (a) dimensionless wave height normalized by $\tilde{R_m}^{p/2}$, (b) dimensionless wavelength normalized by $\tilde{R_m}^{-2q}$ and (c) wave direction relative to the wind. Solid lines are fits (4) and (5) for wind waves and (8), (7) for swell

underdeveloped compared to a stationary TC condition. For moving TCs, wave amplification in the right sector and attenuation in the left one can then result in strong wave field azimuthal asymmetries.

3.1. Wind Wave Development for a Moving TC

Following KYC21b, inside a TC moving with a constant velocity V, fields of wave height H, wavelength λ and wave direction φ, can still be described with self-similar form:

$$\begin{aligned} H/H_0 &= \Phi_H(r/L_{cr}, \theta), \\ \lambda/\lambda_0 &= \Phi_\lambda(r/L_{cr}, \theta), \\ \varphi - \varphi_0 &= \Phi_\varphi(r/L_{cr}, \theta), \end{aligned} \tag{11}$$

where subscript "0" denotes wave parameters for a stationary TC; Φ_H, Φ_λ, and Φ_φ are universal functions of the TC azimuth θ and local radius r, scaled by a local critical fetch L_{cr}:

$$L_{cr} g/u^2 = c_{cr}(u/2V)^{1/q},$$

where c_{cr} is a constant linked to the fetch laws as

$$c_{cr} = -c_\alpha^{-1/q} q/(1+q) = 6.5 \times 10^3$$

with $q = -1/4$ and $c_\alpha = 11.8$ (KYC21a); u the radial wind velocity at given r; g gravity acceleration. The critical fetch defines the distance, from the initial point of wave train generation to the turning point, where the projection of the wave group velocity on the TC heading becomes equal to the TC translation velocity, corresponding to group velocity resonance Young (1988); Dysthe and Harbitz (1987); Kudryavtsev et al. (2015)).

In KYC21b, functions Φ_H, Φ_λ and Φ_φ were represented by numerical matrices generalizing 2D parametric model simulations for different TC parameters: u_m, R_m and V. The self-similar solutions (11) targeted the description of the primary (the longest) wave system parameters. Since the primary wave system can include both wind waves and swell, the solutions (11), essentially based on the fetch law concept, were mostly limited to the TC inner core, $r < 2 - 3R_m$. In this area, a swell system only reached its initial stage, $u_{||}/c_p \sim 1$. In the present development, wind waves and swell are separately considered. This can then include mixed sea conditions. Swell is already described analytically, Eqs.(6). Solutions for the pure wind waves are searched in self-similar form (11), with reference parameters H_0, λ_0 and φ_0, corresponding to a stationary TC, defined by (4)-(5).

The new universal functions-matrices (11) generalize the TC propagation effects, using more than 300 simulations, corresponding to different wind field parameters u_m, R_m, B, and translation velocities V varying from 3 m/s to 12 m/s, Fig. 4. Discussed above, only waves with inverse wave age $u_{||}/c_p > 0.85$ are considered. Functions Φ_H, Φ_λ and Φ_φ on Fig. 4, thus differ from those suggested in KYC21b (their Fig. 18), obtained for the longest waves, i.e. without distinction between pure wind waves or swell. The proposed approach can now apply to any distance $r > R_m$, where the concept of critical fetch makes sense, i.e. where L_{cr} is less than the fetch of fully developed waves, $L_{cr} < a_0^{1/q} c_a^{-1/q} u^2/g$, $a_0 = 0.85$.

At fixed r/L_{cr}, a matrix transect, over a TC azimuth direction, provides azimuthal distributions of the wind waves energy, length and direction, relative to the stationary TC condition, Eqs. (4)-(5). Following KYC21b, the two regimes are defined: "slow", $r/L_{cr} > 1$, when the waves can be "trapped" in the right (left, in the Southern hemisphere) TC sector, and "fast", $r/L_{cr} < 1$, when the TC is too fast with developing waves left behind the TC storm area. Around $r/L_{cr} = 1$, generated waves are subjected to the local group velocity resonance effect, to attain the largest possible energy and wavelength for a given wind field.

Functions Φ_H, Φ_λ, Φ_φ are shown in polar coordinates in Fig. 4. Obtained distributions for H/H_0 and λ/λ_0 are quite similar. Indeed, in terms

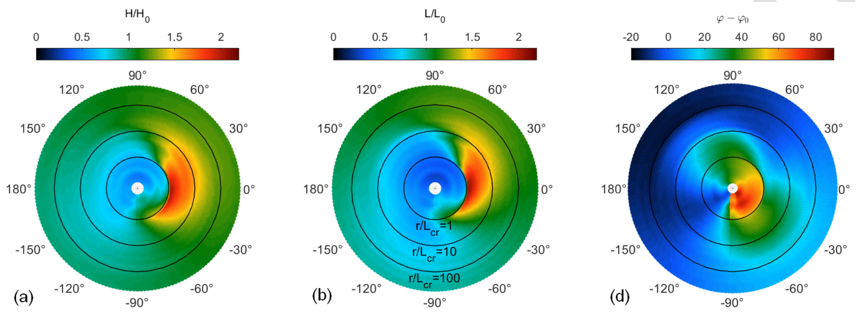

Figure 4: Universal functions (11) for wind wave (a) height, (b) wavelength and (c) peak direction

of extended fetch, X, the self-similar fetch laws read

$$H \sim X_H^{p/2}, \qquad (12)$$
$$\lambda \sim X_\lambda^{-2q},$$

that give close powers (3/8 and 1/2) for $p = 3/4$, $q = -1/4$. At the same time, subplots (a) and (b) in Fig. 4 differ in some details, apparently because the equivalent fetches for wave height and wave length, X_H and X_λ in (12), generally differ for the same TC point (see, e.g. KYC21b, their Eq.18).

Note, functions Φ_H, Φ_λ, Φ_φ, and swell contour matrix C_{sw} presented below, are developed for Northern hemisphere TCs. For Southern hemisphere cases, wind and wave fields are "mirrored" relative to TC heading direction. In Figs. 4-5, the azimuth θ should be reversed, i.e. going in opposite direction. Wind and wave directions, φ_w, φ, φ_0, originally counted counter-clockwise from East, should be counted clockwise in the Southern hemisphere to keep all relations valid.

3.2. Moving TC Swell

3.2.1. Analytical Solutions

Analytical solutions for swell parameters, Eqs. (6), complement wind waves derivation through self-similar matrices. Initial conditions for swell, H_i and λ_i match values of wind waves parameters taken at the distances, on the (r, θ) plane, where wind waves are locally developed, i.e. their inverse wave age is equal to the threshold value 0.85.

To account for wave ray focusing/defocusing effects, the second term in relations (6), the cross-ray gradient of wave directions, $G_{ni} = (d\varphi/dn)_i$, is directly calculated from the wave direction field.

Also note that in a reference system, moving with velocity $\mathbf{V}=(V_x, V_y)$, swell wave-train coordinates (x_{sw}, y_{sw}) are related with swell trajectory length l used in (6):

$$x_{sw} \approx x_i + l\cos\varphi_i(1 - V_x/c_{gx}),$$

$$y_{sw} \approx y_i + l\sin\varphi_i(1 - V_y/c_{gy}),$$

where (x_i, y_i) are initial wave train coordinates at $l = 0$; $\mathbf{c_{gi}}=(c_{gx}, c_{gy})$ is the initial wave group velocity, considered approximately constant along swell trajectory; φ_i is the wave-train propagation direction in geographical reference system.

3.2.2. Swell Radiation Contour

Anticipated for a moving TC, the radius of swell generation R_{sw} is modified compared to a stationary TC conditions. In the right TC sector, developing waves deviate from wind direction outwards from a TC center, but become again aligned with the wind while sliding down in a TC reference system. Thus, a transition to the swell regime occurs at larger radial distances compared to a stationary TC. On the contrary, in the left sector, sliding waves have the direction perpendicular or almost opposite to the wind one, and R_{sw} shortens relative to $R0_{sw}$.

Comparable to functions in Eqs. (11), a self-similar function C_{sw} to define the contour R_{sw} normalized by $R0_{sw}$ (Eq. (9)) is introduced:

$$R_{sw}/R0_{sw} = C_{sw}(R_m/L^m_{cr}, \theta), \quad (13)$$

where L^m_{cr} is the critical fetch defined through maximum wind speed:

$$L^m_{cr} g/u_m^2 = c_{cr}(u_m/2V)^{1/q}.$$

The universal function $C_{sw}(R_m/L^m_{cr}, \theta)$ is obtained by averaging and smoothing the azimuthal radius distributions corresponding to $u_{||}/c_p = 0.85$ versus the dimensionless parameter R_m/L^m_{cr}. A set of simulations is used with different R_m, u_m, B and V. The result is shown Fig. 5. A transect of the matrix C_{sw} along $R_m/Lcr^m = \text{const}$ gives the radius of swell generation $R_{sw}(\theta)$, for a TC with $R_m/Lcr^m > 1$ (only "slow" TCs). For a "fast" TC ($R_m/Lcr^m < 1$),

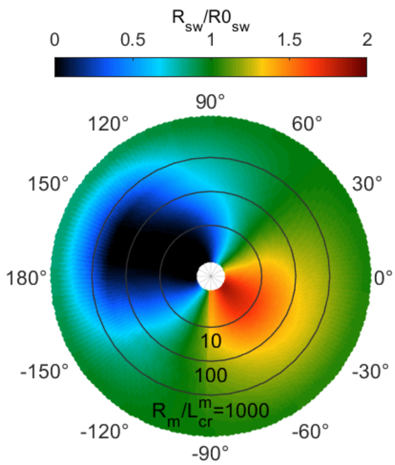

Figure 5: Universal function C_{sw} (Eq. (13)) for the contour of swell generation ($u_{||}/c_p = 0.85$) for a moving TC relative to a stationary TC

the swell contour is not closed, "sliding down" to the backward TC sector. In this region, we can neglect swell waves, small compared to "slow" TC conditions.

Examples of simulated inverse wave age (color) and wave direction (arrows) fields are presented in Fig. 6 for three TCs, corresponding to different combinations of R_m, u_m, B and V (directed to the North). Yellow curves are the contours $u_{||}/c_p = 0.85$ obtained from 2D parametric model calculations. Red ones are those from the self-similar matrix C_{sw}, Eq. (13). Using C_{sw}, predictions quantitatively agree with direct simulations.

However, see the wind waves directions in Fig. 6a,c, contouring wind waves transferring to swell systems cannot always be achieved to cover the whole considered area, more particularly the top-left sector of the TC. From the numerical simulations, swell systems in the top-left sector, travelling at 45 deg to the left from TC heading, originate from wind waves initially developing in the right-top region. Swell can then slide down in the TC reference system, being underneath the longer wind waves developing inside the contour. Further gaining energy and accelerating in the region of maximum winds, these wind waves finally leave the inner area through the contour in the top-left direction propagating as swell. This is not captured in our ap-

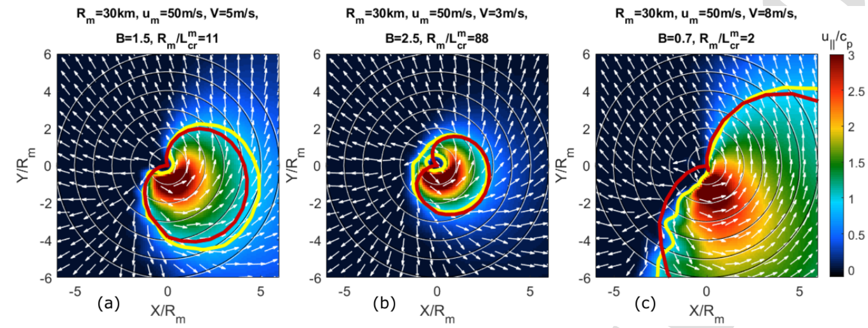

Figure 6: Examples of implementation self-similar function (13) to obtain the contour of swell generation (red curves) in TCs with different parameters (V is directed to the North). Color indicates inverse wave age; arrows show the directions of the longest waves; yellow curves are isolines $u\cos(\varphi - \varphi_w)/c_p = 0.85$ obtained from 2D parametric model simulations

proach using the criterion $u_{||}/c_p = 0.85$ for the longest waves in each grid cell. However, in some simulations, e.g. on Fig. 6b, such waves still continue their development as wind waves in the left half-space relative to TC heading. In this case, the two contours $u_{||}/c_p = 0.85$ are distinguished, the outer one providing swell propagating in the top-left direction.

To take into account these waves for all cases, we artificially extend the contour obtained trough Eq. (13) by adding a condition $R_{sw} = \max(R_{sw}, 1.5R_m)$. We hypothesize that, at $r = 1.5R_m$, initial swell parameters, derived from the universal matrices, are close to observed ones in the top-left sector. Indeed, in this region, Φ_H, Φ_λ, Φ_φ are determined from cases comparable to Fig. 6b, where comparable swell waves are formed.

4. Model Summary

A flowchart explaining the model calculation procedure is presented Fig. 7. Input parameters come from the TC axi-symmetric wind field (1), with maximum wind speed u_m, radius of maximum winds R_m, shape parameter B, and 20^o inflow angle. The wind field is moving with translation velocity V.

First, sets of reference parameters, $H_0, \lambda_0, \varphi_0$, from stationary TC condition ($V = 0$), are calculated using Eq. (4) for the energy and wavelength and Eq. (5) for the wave direction.

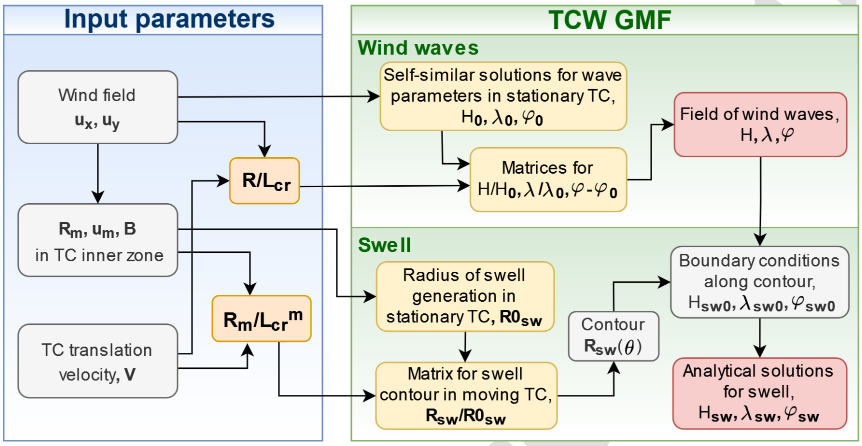

Figure 7: Scheme to derive the fields of wind waves and swell systems using TCW GMF

For a moving TC, Wind wave height (H), wavelength (λ) and direction (φ) are described by self-similar solutions (11), numerically derived Fig. 4. The contour $R_{sw}(\theta)$ marking the transition from wind waves to swell transition is then determined, using (13) and (9), also numerically derived (Fig. 5). H, λ and φ from self-similar solutions (11) along the transition contour, are then used as boundary conditions (H_{sw0}, λ_{sw0} and φ_{sw0}) in analytical expressions to determine swell parameters H_{sw}, λ_{sw} and φ_{sw}. Swell direction is considered constant along its trajectory, equal to that at its initial contour origin.

Superposition of wind waves and swell represents mixed sea condition. Following KYC21b, we term this self-similar model as TC-Wave Geophysical Model Function (TCW GMF).

Numerical tables for all 2D self-similar functions and MATLAB examples of TCW GMF implementation in any Earth hemisphere are available online at https://doi.org/10.5281/zenodo.6970690.

5. Validation

5.1. Wind and Wave Data

To test the TCW GMF, multi-satellite altimeter measurements, accumulated within TC regions during the period January 2020 to March 2022, are considered. Level-3 along-track products, significant wave height and wind speed, from 7 altimeters (AltiKa, CryoSat-2, CFOSAT, HaiYang-2B, Jason-3, Sentinel-3A, Sentinel-3B) are available through the Copernicus Marine Service (https://resources.marine.copernicus.eu/products). TCs coordinates every 3 hours and wind field information (maximum wind speed, radius of maximum winds and, if available, radii of 30, 34, 50 and 64 kn winds in different TC quadrants) are taken from the Best Track Data (International Best Track Archive for Climate Stewardship (IBTrACS), https://www.ncdc.noaa.gov/ibtracs/), to fit wind profile by the Holland model (1). TC eye locations are used to estimate TC translation velocity.

Resulting 2D wind fields are axi-symmetrical with 20^o inflow angle, i.e. wind information from all 4 quadrants are equally weighted to approximate the wind profile. The original main TC parameters, u_m and R_m from the Best Track Data are averaged over the previous 12 hours. Thus, the approximation procedure reduces to estimate the parameter B, restricted to range from 0.5 to 2.5.

In some cases, the wind profile cannot exactly be fitted with function (1), e.g. the same parameters u_m, R_m, B cannot adjust to match both the inner and outer TC zones. To solve this problem, these regions are treated separately. For the inner part, wind data (r30, r34, r50, r64) were weighted with inverse distance from TC center $1/r$, and at the periphery they were weighted with r. The maximum wind was always kept at distance R_m from TC eye, but unfixed and limited by $(0.9-1)u_m$ in the near zone and $(0.5-1)u_m$ in the far zone. The envelope of these two fits, i.e. the maximum wind speed at each radius, then is treated to be the desirable wind profile.

Only TCs, with maximum winds higher than 30 m/s are further considered. In total, 95 TC cases were collected, their trajectories shown Fig. 8. Altimeter track segments are selected to cross the TC area within 600 km to the eye. This dataset, combining wind parameters, including wind profile parameterization, and altimeter-derived wave information in TC regions is freely available at https://doi.org/10.5281/zenodo.6795330.

Among more than 2000 tracks, 708 were kept, for which TC parameters were quite stable during the previous 12-24 hours. For these selected cases, wind information is sufficient to model the wind profile, and waves are not shielded by islands or coast.

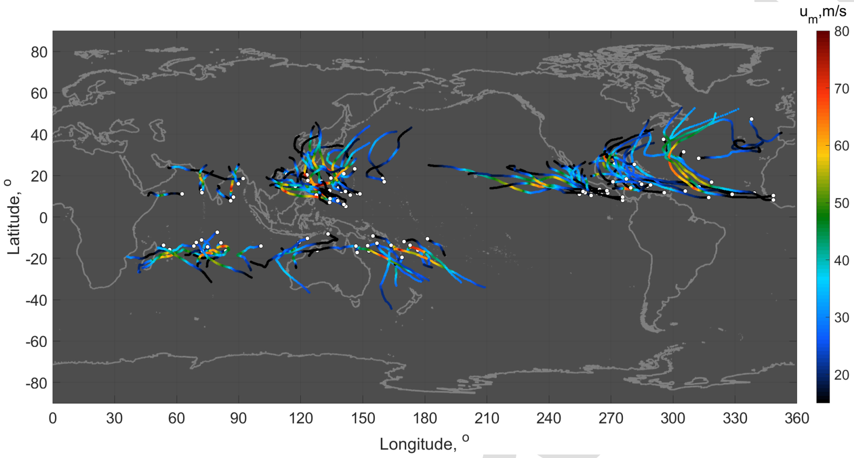

Figure 8: Trajectories of the most intensive TCs from January 2020 to March 2022. Color is maximum wind speed, white circles are TCs' origins, according to the Best Track Data

5.2. Model Results and Observations

First, a quasi-stationary TC case is considered. Formed over the Indian Ocean in March 2021, TC Marian propagated with a very low velocity. At its most intensive stage, TC Marian reaches maximum wind speed up to 50 m/s, with heading velocity about 1 m/s. Jason-3 track passed ∼100 km away from the TC center, Fig. 9a. The Best Track parameters, averaged over the previous 12 hours, give $u_m = 46$ m/s, $R_m = 32$ km, and wind profile approximation (1) gives $B = 0.98$, Fig. 9b. Wind vectors were directed clockwise as assigned to TCs in Southern hemisphere.

Wind wave Hs and wavelength fields obtained from self-similar solutions (11) are shown Fig. 9c,f. Owing to small TC heading velocity, these fields are almost symmetrical. The largest TC-generated waves develop to about 7 m with wavelengths ∼200 m. Taking into account swell waves, starting from contour (13), Fig. 9d,g, brings excellent agreement with altimeter-measured Hs, Fig. 9e. TCW GMF-derived Hs and wavelength fields are close to that obtained from direct KYC21a wave-ray simulations, Fig. 9i,j, where rays are superimposed so that the longest waves lie atop the shorter ones. Maximum Hs and wavelength predictions also agree with Young (2017) (or Young and Vinoth (2013)) extended fetch model with input parameters R_m=32 km;

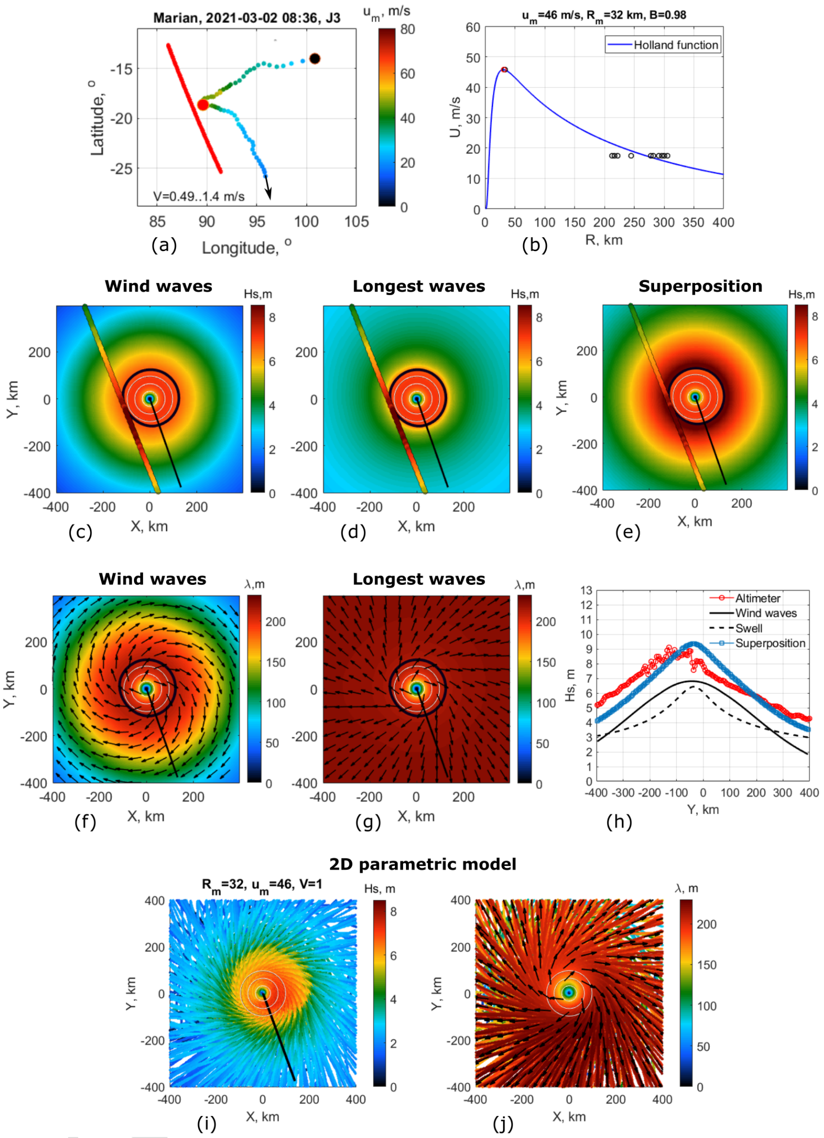

Figure 9: (a) Trajectory of TC Marian (color circles) and track of altimeter Jason-3 altimeter; red circle is TC location at the time of altimeter measurements. (b) Circles: wind speed from Best Track Data during previous 12 hours before altimeter passage; blue line is fit (1) of wind profile. TCW GMF-derived fields of wind waves Hs (c) and wavelength (f), longest waves Hs (d) and wavelength (g); superposition of wind waves and swell (e). Black contours in (c)-(g) are R_{sw} (13), black solid lines indicate TC heading direction. (h) Along-track Hs profiles for modeled wind waves (solid black), swell (dashed black) and their superposition (blue) compared with altimeter Hs measurements (red). KYC21a model simulations of (i) wave height and (j) wave length for this TC

u_m=46 m/s and V=1 m/s, giving 7.4 and 152 m, respectively.

Along-track wave height profiles are shown in more detail in Fig. 9h. Illustrated, Hs of wind waves (black solid line) and swell (dashed) have close magnitudes, ranging from 3 m at the periphery to 5 m closer to the TC center. Their superposition (blue symbols) gives values qualitatively and quantitatively (within 20% accuracy) consistent with altimeter-derived Hs (red).

An other case, TC Larry, formed in North Atlantic in September 2021, is presented Fig. 10. This TC attained wind speeds up to 55 m/s. At the moment of Jason-3 acquisitions, TC Larry was moving with velocity 4 m/s, being a typical example of "slow TC" ($R_m/L_{cr}^m \approx 80$). The wind profile could not be accurately fitted with single function (1), with a marked sharp wind decay, followed by a saturation at ∼20 m/s at radii 150-300 km, Fig. 10a. Thus, two profiles with u_m = 55 m/s, R_m = 74 km, B = 2.5 and u_m = 36 m/s, R_m = 74 km, B = 1.4, were merged to fit the wind observations. The envelope of these profiles was then used to input the TCW GMF.

Larry's TCW GMF-reconstructed wind waves fields reveal expected strong azimuthal asymmetry with maximum waves in the right (North) quadrant, reaching 15 m height and 350 m wavelength, Fig. 10c,f. Again, this is in agreement both with full KYC21a simulations, Fig. 10i,j and Young (2017) extended fetch model prediction of maximum Hs and wavelength (15.1 and 332 m, respectively), as well as with Young (1988) H/Hmax distributions, Fig. 10k (note that these simulations were performed for a TC moving upward).

Swell contour is also asymmetric, stretched to the right-backward sector. The longest 350 m swell waves are radiated in the East direction, Fig. 10g. Superposition of wind waves and swell is shown Fig. 10e, and Hs transects along the altimeter track are given Fig. 10h. For this TC case, the energy of wind waves, several radii ahead the TC center, is dominated by its swell counterpart, i.e. compare black solid and dashed lines in Fig. 10h. The measured Hs can solely be attributed to swell. Here, the local wind sea is fully developed, as confirmed using the Pierson-Moskovitz (Pierson and Moskowitz (1964)) expression for the height H_{PM} of fully developed waves under the action of constant wind u:

$$H_{PM} = 0.21u^2/g, \tag{14}$$

with local wind speed taken from the altimeter product, gray circles in

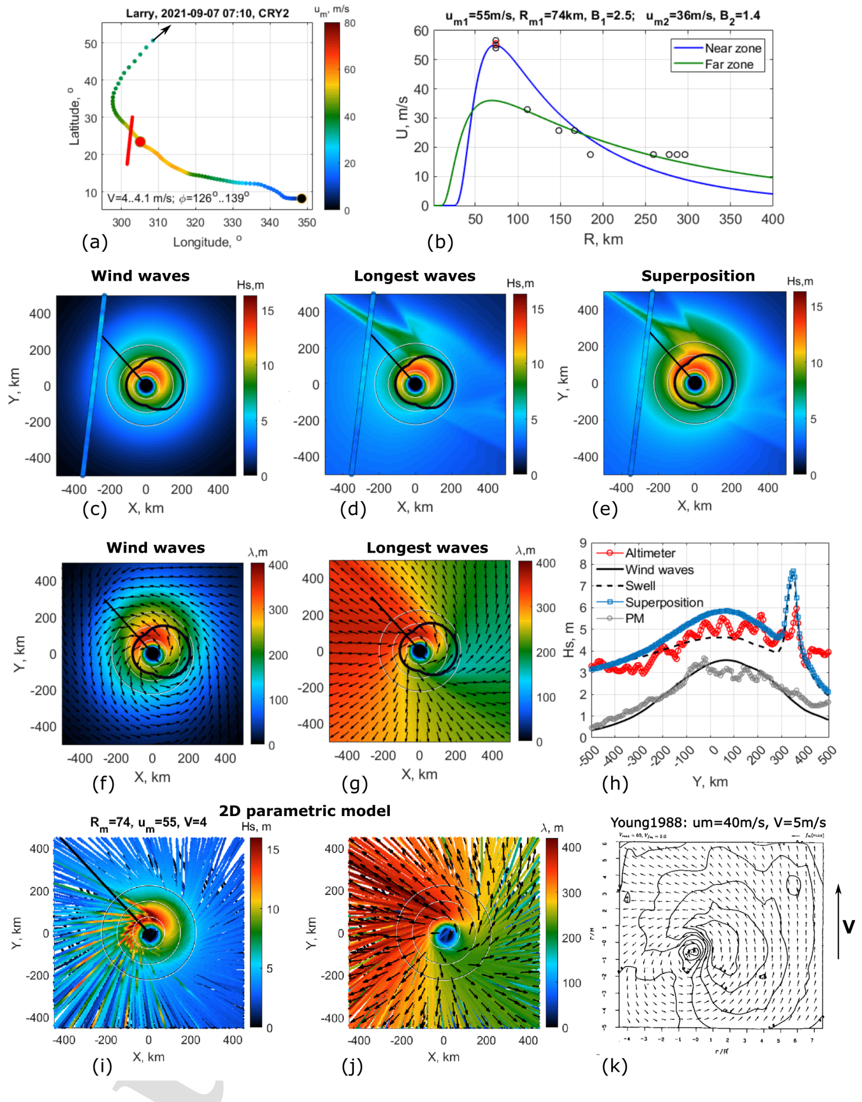

Figure 10: (a) Trajectory of TC Larry (color circles) and track of altimeter CryoSat-2; red circle is TC location at the time of altimeter measurements. (b) Circles: wind speed from Best Track Data during previous 12 hours before altimeter passage; solid curves are fit (1) for inner (blue) and far (green) TC zones. TCW GMF-derived fields of wind waves Hs (c) and wavelength (f), longest waves Hs (d) and wavelength (g); superposition of wind waves and swell (e). Black contours in (c)-(e) are R_{sw} (13), black solid lines indicate TC heading direction. (h) Along-track Hs profiles for modeled wind waves (solid black), swell (dashed black) and their superposition (blue) compared with altimeter Hs measurements (red). Gray circles are the upper estimate of wind waves (14) from altimeter-derived wind speed. (i)-(j) KYC21a wave-ray simulations of wave height and wave length for this TC and (k) normalized significant wave height and mean wave direction distributions for a TC with similar parameters moving upwards (figure from Young (1988))

Fig. 10h. The overall consistency with the along-track modeled wind waves confirms the TCW GMF good performance.

Further note an interesting feature of swell wave field predicted by TCW GMF, Fig. 10d - energy intensification in the North-East direction due to ray focusing effect. A similar peculiarity is seemingly revealed in the altimeter measurements, see along-track Hs profile (red) in Fig. 10h at $Y = 350 - 400$ km. Though local peak in Hs measurements is not well expressed, we may still speculate that it originates from swell ray focusing. At large distance, this effect can also be masked due to deviation of swell trajectories, e.g. swell refraction in the presence of intense ocean currents.

Hurricane Niran, rapidly traveling in South Pacific at its terminal stage on 7th March 2021, Fig. 11, is a "fast" TC case. Its translation velocity varied from 10 to 21 m/s, giving $R_m/L_{cr}^m \ll 1$ for $R_m = 47$ km and $u_m = 32$ m/s. TC trajectory, track of altimeter CryoSat-2 and fit (1) of the Best Track wind data are shown Fig. 11a,b. As developed, only the wind wave field can be assessed through TCW GMF for "fast" TCs, Fig. 11c,d. Maximum waves in these TCs "slide down" to the right-backward quadrant (left-backward in Southern hemisphere) relative to TC heading. Sea state usually does not reach very large Hs and wavelength values (6 m and 150 m, respectively in the case of Niran). Direct model simulations, Fig. 11f,g, generally predict the same Hs and wave length magnitudes, but slightly differ at the TC periphery in the back sector providing more detailed and complicated wave-ray distributions. Wave height distributions for a similar TC, suggested by Young (1988), Fig. 11h (plotted for Northern hemisphere and TC moving upward), and Young (2017) estimates of maximum wave height and wavelength, 6.6 m and 154 m, respectively, also correspond well to TCW GMF and KYC21a results. Altimeter track passed 200 km ahead the TC where both modeled and measured Hs give consistent values around 2-3 m, Fig. 11e.

Finally, a scatter plot comparing modeled and observed Hs along all 703 selected altimeter tracks is presented, Fig. 12. Color indicates the number of data points in a given 25x25 cm wave height range. Obtained correlation coefficient is 0.84 and root mean square error is 1.1 m with no significant bias.

5.3. Model limitations

To recall, the TCW GMF is developed to provide simple first guess estimates of wave fields generated by an arbitrary TC in deep water, neglecting surface current effects. TCW GMF predictions are not intended to compete

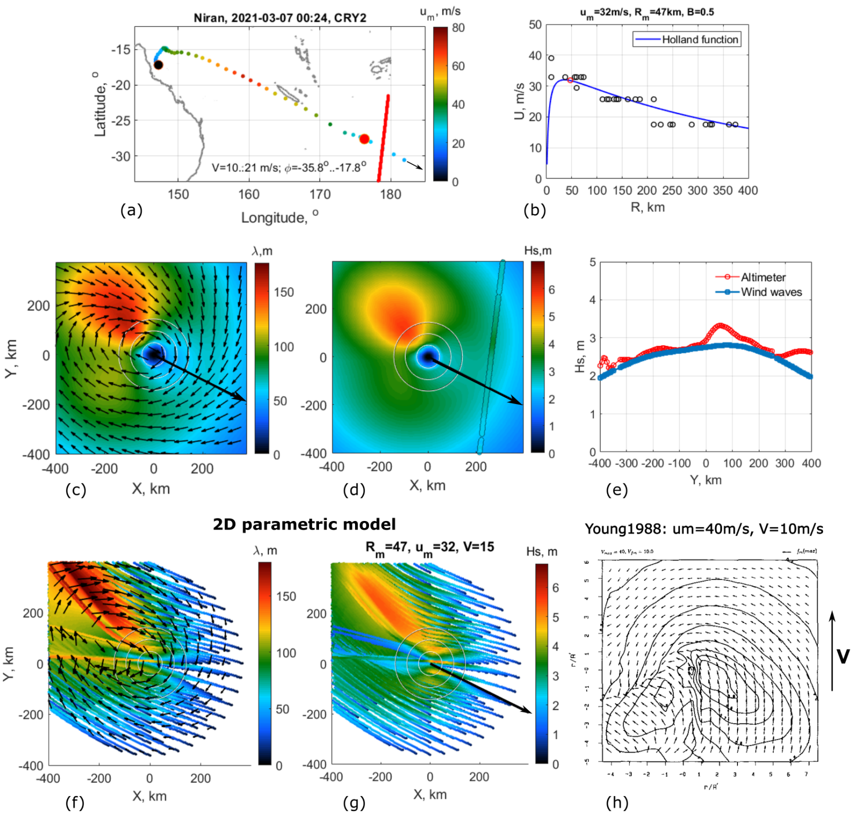

Figure 11: (a) Trajectory of TC Niran (color circles) and track of altimeter CryoSat-2 (red solid line); red circle is TC location at the time of altimeter measurements. (b) Circles: wind speed from Best Track Data during previous 12 hours before altimeter passage; blue line is fit (1) of wind profile. TCW GMF-derived fields of wind waves wavelength (c) and Hs (d); black solid lines indicate TC heading direction. (h) Along-track profiles of modeled (blue) and measured (red) Hs. KYC21a wave-ray simulations of (f) wavelength and (g) wave height for this TC and (h) normalized significant wave height and mean wave direction for a TC with similar parameters moving upward in Northern hemisphere (figure from Young (1988))

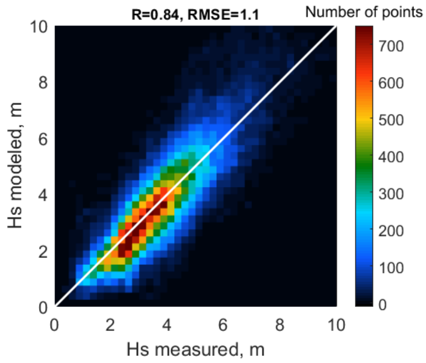

Figure 12: Scatter plot for TCW GMF- and altimeter-derived significant wave height along 708 altimeter tracks in 95 TCs

with advanced wind wave generation models or even with full 2D parametric model (KYC21a). Thus, to derive and test the self-similar functions, quite rough assumptions can be accepted, especially regarding the axi-symmetric wind field and constant (averaged) values of wind profile parameters, TC heading velocity and direction for the whole period of waves development. Nonetheless, Fig. 12 demonstrates an overall convincing agreement of TCW GMF predictions with observed Hs values. It proves the method robustness and can then be used for rapid ensemble estimations and/or comparisons with satellite observations.

Being fast and easy to use, TCW GMF provides a steady solution for waves developing under the same conditions for at least 12 hours, and thus, it cannot correctly reproduce the wave fields in complicated situations, when TC trajectory is far from a strait line during this time, or if the wind field changes rapidly, and also in the very beginning of TC evolution. The solutions are not applicable if the wind profile differs significantly from Holland-like function. The result can also be imprecise if the wind inflow angle differs much from 20^o, as assumed in this study, or if the wind angular distribution is strongly asymmetrical - in this case the wave field is mostly determined by the wind shape in left quadrant. Besides this, TCW GMF can underestimate the waves in a TC eye, $r < R_m$, as swell originated in the right-up quadrant is considered only at radii starting from $1.5R_m$.

In all these situations either full KYC21a model (example of its implementation in arbitrary space and time varying wind conditions is given in Kudryavtsev et al. (2022)) or advanced spectral models like WAM and WAVEWATCH-III can be preferable.

6. Summary

Simple self-similar solutions, termed Tropical Cyclone-Wave Geophysical Model Function (TCW GMF) to describe wave fields generated by a TC have been derived.

First, wave parameters for stationary TC conditions are calculated. Solutions are found similar to classical fetch laws for the wind wave development, with the radial distance from TC center replacing the fetch definition. Radial profiles of the wind wave heights, wavelengths and direction, obtained for stationary TC conditions, are considered as the reference ones. These solutions are then further used to derive parameters for moving TC conditions. Self-similar functions-matrices are derived, generalizing 2D parametric model simulations with different TC parameters (maximum wind speed, cyclone radius, wind shape parameter B and TC translation velocity). Compared to previous developments (KYC21b), this new version of TCW GMF is now valid at larger distances from the TC eye, including the TC outer periphery. It can also better account for the wave field sensitivity to the shape of the wind profile.

Wind waves distributions are completed with analytical description of swell emitted away from the TC intense area, emanating along a contour marking the wind waves-to-swell transition. This contour is defined from the universal function-matrix, providing boundaries where the local inverse wave age of wind waves reaches the threshold value $u_{||}/c_p = 0.85$.

These proposed self-similar solutions were validated using more than 700 altimeter measurements with tracks crossing different TCs during the 2020-2022 period. Best Track Data were used to derive the guess wind profile, TC's coordinates and translation velocity. Comparisons between modeled and measured wave heights demonstrate encouraging consistency.

Suggested TCW GMF efficiently thus provides immediate first-guess estimates of 2D surface wave distributions (Hs, wavelength and direction of wind waves and swell). The model offers a relative computation simplicity, and can be used as an auxiliary instrument for different scientific and practical applications, i.e. to perform ensembles using varied input TC parameters, to improve understandings and predictions of surface wave generation under extreme wind conditions, and/or to assess wave dissipation and breaking impacts on the vertical mixing intensity in the upper ocean upper (e.g. Chukharev and Pavlov (2021); Kudryavtsev et al. (2019)). First guess wave fields can also be used to analyze high resolution synthetic aperture radar (SAR) scenes, acquired during extreme conditions (Mouche et al. (2019); Combot et al. (2020)), to help advance improved retrieval algorithms, and more precisely monitor and predict wave evolution across ocean basins (Ardhuin et al. (2009); Collard et al. (2009)).

For users' convenience all the universal numerical matrices and TCW GMF MATLAB code are freely available at https://doi.org/10.5281/zenodo.6970690.

Acknowledgements

The core support for this work was provided by the Russian Science Foundation Grant No. 21-17-00236. The support of the Ministry of Science and Education of the Russian Federation under State Assignment No. FNNN-2021-0004 at MHI RAS (provision of information and computing resources in development of a TC dataset) and State Assignment No. 0736-2020-0005726 at RSHU (numerical simulations using 2D parametric model) are gratefully acknowledged. This study is also supported by the ESA OCEAN+EXTREME MAXSS project C.N.4000132954/20/I-NB and ESA Contract No. 4000135827/21/NL - Harmony Science Data Utilisation and Impact Study for Ocean.

References

Aouf, L., Hauser, D., Chapron, B., Toffoli, A., Tourain, C., Peureux, C., 2021. New directional wave satellite observations: Towards improved wave forecasts and climate description in southern ocean. Geophysical Research Letters 48, e2020GL091187. URL: https://agupubs.onlinelibrary.wiley.com/doi/abs/10.1029/2020GL091187, doi:https://doi.org/10.1029/2020GL091187, arXiv:https://agupubs.onlinelibrary.wiley.c e2020GL091187 2020GL091187.

Ardhuin, F., Chapron, B., Collard, F., 2009. Observation of swell dissipation across oceans. Geophysical Research Letters 36. URL: https://agupubs.onlinelibrary.wiley.com/doi/abs/10.1029/2008GL037030, doi:https://doi.org/10.1029/2008GL037030, arXiv:https://agupubs.onlinelibrary.wiley.c

Babanin, A.V., Rogers, W.E., de Camargo, R., Doble, M., Durrant, T., Filchuk, K., Ewans, K., Hemer, M., Janssen, T., Kelly-Gerreyn, B., Machutchon, K., McComb, P., Qiao, F., Schulz, E., Skvortsov, A., Thomson, J., Vichi, M., Violante-Carvalho, N., Wang, D., Waseda, T., Williams, G., Young, I.R., 2019. Waves and swells in high wind and extreme fetches, measurements in the southern ocean. Frontiers in Marine Science 6. URL: https://www.frontiersin.org/article/10.3389/fmars.2019.00361, doi:10.3389/fmars.2019.00361.

Babanin, A.V., Soloviev, Y.P., 1998. Field investigation of transformation of the wind wave frequency spectrum with fetch and the stage of development. Journal of Physical Oceanography 28, 563 – 576. doi:10.1175/1520-0485(1998)028¡0563:FIOTOT¿2.0.CO;2.

Badulin, S.I., Babanin, A.V., Zakharov, V.E., Resio, D., 2007. Weakly turbulent laws of wind-wave growth. Journal of Fluid Mechanics 591, 339–378. doi:10.1017/S0022112007008282.

Badulin, S.I., Zakharov, V.E., 2017. Ocean swell within the kinetic equation for water waves. Nonlinear Processes in Geophysics 24, 237–253. URL: https://npg.copernicus.org/articles/24/237/2017/, doi:10.5194/npg-24-237-2017.

Booij, N., Ris, R.C., Holthuijsen, L.H., 1999. A third-generation wave model for coastal regions: 1. model description and validation. Journal of Geophysical Research: Oceans 104, 7649–7666. URL: https://agupubs.onlinelibrary.wiley.com/doi/abs/10.1029/98JC02622, doi:https://doi.org/10.1029/98JC02622, arXiv:https://agupubs.onlinelibrary.wiley.com/

Bowyer, P.J., MacAfee, A.W., 2005. The theory of trapped-fetch waves with tropical cyclones—an operational perspective. Weather and Forecasting 20, 229–244.

Bretschneider, C., 1959. Hurricane design—wave practices. Trans. ASCE 124, 39–62.

Chukharev, A.M., Pavlov, M.I., 2021. Model and experimental estimates of vertical mixing intensity in the sea upper homogeneous layer. Physical Oceanography 28, 309–325.

Collard, F., Ardhuin, F., Chapron, B., 2009. Monitoring and analysis of ocean swell fields from space: New methods for routine observations. Journal of Geophysical Research 114.

Combot, C., Mouche, A., Knaff, J., Zhao, Y., Vinour, L., Quilfen, Y., Chapron, B., 2020. Extensive high-resolution synthetic aperture radar (sar) data analysis of tropical cyclones: comparisons with sfmr flights and best-track. Monthly Weather Review 148, 4545–4563. doi:10.1175/MWR-D-20-0005.1.

Dysthe, K.B., Harbitz, A., 1987. Big waves from polar lows? Tellus A: Dynamic Meteorology and Oceanography 39, 500–508. doi:10.3402/tellusa.v39i5.11776, arXiv:https://doi.org/10.3402/tellusa.v39i5.11776.

Hasselmann, K., 1962. On the non-linear energy transfer in a gravity-wave spectrum part 1. general theory. Journal of Fluid Mechanics 12, 481–500. doi:10.1017/S0022112062000373.

Hasselmann, K., Hasselmann, K., Bauer, E., Janssen, P., Komen, G., Bertotti, L., Lionello, P., Guillaume, A., Cardone, V., Greenwood, J., Reistad, M., Zambresky, L., Ewing, J., 1988. The wam model - a third generation ocean wave prediction model. Journal of Physical Oceanography 18, 1775–1810.

Hauser, D., Tourain, C., Hermozo, L., Alraddawi, D., Aouf, L., Chapron, B., Dalphinet, A., Delaye, L., Dalila, M., Dormy, E., Gouillon, F., Gressani, V., Grouazel, A., Guitton, G., Husson, R., Mironov, A., Mouche, A., Ollivier, A., Oruba, L., Piras, F., Rodriguez Suquet, R., Schippers, P., Tison, C., Tran, N., 2021. New observations from the swim radar on-board cfosat: Instrument validation and ocean wave measurement assessment. IEEE Transactions on Geoscience and Remote Sensing 59, 5–26. doi:10.1109/TGRS.2020.2994372.

Holland, G.J., 1980. An analytic model of the wind and pressure profiles in hurricanes. Monthly Weather Review 108, 1212–1218. doi:10.1175/1520-0493(1980)108¡1212:AAMOTW¿2.0.CO;2.

Kalourazi, M.Y., Siadatmousavi, S.M., Yeganeh-Bakhtiary, A., Jose, F., 2021. Wavewatch-iii source terms evaluation for optimizing hurricane wave modeling: A case study of hurricane ivan. Oceanologia 63, 194–213. URL: https://www.sciencedirect.com/science/article/pii/S0078323420301111, doi:https://doi.org/10.1016/j.oceano.2020.12.001.

King, D., Shemdin, O., 1987. Radar observations of hurricane wave directions. In 16th International Confession on Coastal Engineering; Hamburg, Germany, 1978; ASCE: Hamburg, Germany , 209–226.

Kitaigorodski, S., 1962. Applications of the theory of similarity to the analysis of wind-generated wave motion as a stochastic process. Bulletin of the Academy of Sciences of the USSR Geophysics Series 1, 105–117.

Kudryavtsev, V., Cheshm Siyahi, V., Yurovskaya, M., Chapron, B., 2022. On Surface Waves in Arctic Seas. Boundary-Layer Meteorology doi:10.1007/s10546-022-00768-9.

Kudryavtsev, V., Golubkin, P., Chapron, B., 2015. A simplified wave enhancement criterion for moving extreme events. Journal of Geophysical Research: Oceans 120, 7538–7558. URL: https://agupubs.onlinelibrary.wiley.com/doi/abs/10.1002/2015JC011284, doi:https://doi.org/10.1002/2015JC011284.

Kudryavtsev, V., Monzikova, A., Combot, C., Chapron, B., Reul, N., Yves, Q., 2019. A simplified model for the baroclinic and barotropic ocean response to moving tropical cyclones: 1. satellite observations. Journal Of Geophysical Research-oceans 124, 3446–3461. URL: https://archimer.ifremer.fr/doc/00491/60252/, doi:https://doi.org/10.1029/2018JC014746.

Kudryavtsev, V., Yurovskaya, M., Chapron, B., 2021a. 2D Parametric Model for Surface Wave Development Under Varying Wind Field in Space and Time. Journal of Geophysical Research (Oceans) 126, e16915. doi:10.1029/2020JC016915.

Kudryavtsev, V., Yurovskaya, M., Chapron, B., 2021b. Self Similarity of Surface Wave Developments Under Tropical Cyclones. Journal of Geophysical Research (Oceans) 126, e16916. doi:10.1029/2020JC016916.

Mouche, A., Chapron, B., Knaff, J., Zhao, Y., Zhang, B., Combot, C., 2019. Copolarized and cross-polarized sar measurements for high-resolution description of major hurricane wind structures: Application to irma category 5 hurricane. Journal of Geophysical Research: Oceans 124, 3905–3922. URL: https://agupubs.onlinelibrary.wiley.com/doi/abs/10.1029/2019JC015056, doi:https://doi.org/10.1029/2019JC015056.

Pierson, Willard J., J., Moskowitz, L., 1964. A Proposed Spectral Form for Fully Developed Wind Seas Based on the Similarity Theory of S. A. Kitaigorodskii. Journal of Geophysical Research: Oceans 69, 5181–5190. doi:10.1029/JZ069i024p05181.

Shimura, T., Mori, N., Urano, D., Takemi, T., Mizuta, R., 2022. Tropical Cyclone Characteristics Represented by the Ocean Wave-Coupled Atmospheric Global Climate Model Incorporating Wave-Dependent Momentum Flux. Journal of Climate 35, 499–515. doi:10.1175/JCLI-D-21-0362.1.

Tao, D., Bell, M., Rotunno, R., van Leeuwen, P.J., 2020. Why do the maximum intensities in modeled tropical cyclones vary under the same environmental conditions? Geophysical Research Letters 47, e2019GL085980. URL: https://agupubs.onlinelibrary.wiley.com/doi/abs/10.1029/2019GL085980, doi:https://doi.org/10.1029/2019GL085980, arXiv:https://agupubs.onlinelibrary.wiley.c e2019GL085980 2019GL085980.

Tolman, H.L., 2009. User manual and system documentation of wavewatch iii version 3.14 (tech. note 276). Camp Springs, MD: NOAA/NWS/NCEP/MMAB , 194.

Young, I.R., 1988. Parametric hurricane wave prediction model. Journal of Waterway, Port, Coastal, and Ocean Engineering 114, 637–652. doi:10.1061/(ASCE)0733-950X(1988)114:5(637).

Young, I.R., 2006. Directional spectra of hurricane wind waves. Journal of Geophysical Research: Oceans 111. URL: https://agupubs.onlinelibrary.wiley.com/doi/abs/10.1029/2006JC003540, doi:https://doi.org/10.1029/2006JC003540, arXiv:https://agupubs.onlinelibrary.wiley.c

Young, I.R., 2017. A review of parametric descriptions of tropical cyclone wind-wave generation. Atmosphere 8. URL: https://www.mdpi.com/2073-4433/8/10/194, doi:10.3390/atmos8100194.

Young, I.R., Vinoth, J., 2013. An "extended fetch" model for the spatial distribution of tropical cyclone wind-waves as observed by altimeter. Ocean Engineering 70, 14–24.

Yurovskaya, M., Kudryavtsev, V., Mironov, A., Mouche, A., Collard, F., Chapron, B., 2022. Surface wave developments under tropical cyclone goni (2020): Multi-satellite observations and parametric model comparisons. Remote Sensing 14. URL: https://www.mdpi.com/2072-4292/14/9/2032, doi:10.3390/rs14092032.

Zakharov, V.E., Badulin, S.I., Geogjaev, V.V., Pushkarev, A.N., 2019. Weak-turbulent theory of wind-driven sea. Earth and Space Science 6, 540–556. URL: https://agupubs.onlinelibrary.wiley.com/doi/abs/10.1029/2018EA000471, doi:https://doi.org/10.1029/2018EA000471.

Zaslavskii, M.M., 2000. Nonlinear evolution of the spectrum of swell. Izv. Atmos. Ocean. Phys. 36, 253–260.

Zhang, J.A., Uhlhorn, E.W., 2012. Hurricane sea surface inflow angle and an observation-based parametric model. Monthly Weather Review 140, 3587 – 3605. URL: https://journals.ametsoc.org/view/journals/mwre/140/11/mwr-d-11-00339.1.xml, doi:10.1175/MWR-D-11-00339.1.

Author Statement

All persons who meet authorship criteria are listed as authors, and all authors certify that they have participated sufficiently in the work to take public responsibility for the content, including participation in the concept, design, analysis, writing, or revision of the manuscript.

Each author certifies that this material or similar material has not been and will not be submitted to or published in any other publication before its appearance in the Journal of Ocean Modelling.

All authors have read and agreed to the published version of the manuscript.

Author Contributions:

Maria Yurovskaya: formulation of research goals and aims; methodology; software development; data collection; validation; writing the initial and revised draft

Vladimir Kusryavtsev: conceptualization; formulation and evolution of research goals and aims; methodology; formal analysis; writing: review and editing

Bertrand Chapron: conceptualization; writing: review and editing

Declaration of interests

☒The authors declare that they have no known competing financial interests or personal relationships that could have appeared to influence the work reported in this paper.

☐The authors declare the following financial interests/personal relationships which may be considered as potential competing interests: